Transcranial photoacoustic imaging of NMDA-evoked focal circuit dynamics in rat forebrain

Jeeun Kang[1, 2], Shilpa D. Kadam[3], Joshua S. Elmore[1], Brennan J. Sullivan[4,*], Heather Valentine[1,*], Adarsha P. Malla[5], Maged M. Harraz[5], Arman Rahmim[1], Jin U. Kang[2, 6], Leslie M. Loew[7], Michael Baumann[8], Anthony A. Grace[9], Albert Gjedde[1,10,11,12], Emad M. Boctor[1,2,6, 13,†], Dean F. Wong[1,5,14,15 †]

[1] Russell H. Morgan Department of Radiology and Radiological Science, Johns Hopkins University, Baltimore, MD, USA.

[2] Laboratory of Computational Sensing and Robotics, Whiting School of Engineering, Johns Hopkins University, Baltimore, MD, USA

[3] Neuroscience Laboratory, Hugo W. Moser Research Institute at Kennedy Krieger & Department of Neurology, Johns Hopkins Medical Institutions, Baltimore, MD, USA

[4] Neuroscience Laboratory, Hugo W. Moser Research Institute at Kennedy Krieger, Baltimore, MD, USA

[5] The Solomon H. Snyder Department of Neuroscience, Johns Hopkins University School of Medicine, Baltimore, MD, USA

[6] Department of Electrical and Computer Engineering, Whiting School of Engineering, Johns Hopkins University, Baltimore, MD, USA

[7] Department of Cell Biology, University of Connecticut Health, Farmington, CT, USA

[8] National Institute on Drug Abuse, Intramural Research Program, NIH, Baltimore, MD

[9] Departments of Neuroscience, Psychiatry and Psychology, University of Pittsburgh, Pittsburgh, PA, USA

[10] Department of Neurology and Neurosurgery, McGill University, Montreal, Quebec, Canada

[11] Departments of Clinical Research and Nuclear Medicine, Odense University Hospital and University of Southern Denmark, Odense, Denmark

[12] Department of Neuroscience, University of Copenhagen, Copenhagen, Denmark

[13] Department of Computer Science, Whiting School of Engineering, Johns Hopkins University, Baltimore, MD, USA

[14] Department of Psychiatry and Behavioral Sciences, Johns Hopkins Medical Institutions, Baltimore, MD, USA

[15] Department of Neurology, Johns Hopkins Medical Institutions, Baltimore, MD, USA

*** Equal contribution**

† These authors share senior authorship and address all correspondence to: Dean F. Wong, E-mail: dfwong@jhmi.edu and to Emad M. Boctor, E-mail: eboctor1@jhmi.edu;

Keywords: Photoacoustic, neuroimaging, voltage-sensitive dye imaging, microdialysis, quantitative encephalopathy, N-methyl-D-aspartate, glutamate, motor cortex, hippocampus

Abstract

Transcranial photoacoustic (PA) voltage-sensitive dye (VSD) imaging promises to overcome current temporal and spatial limitations of functional neuroimaging. The technique previously distinguished global seizure activity from control neural activity in groups of rats. To validate the focal specificity of transcranial PA with VSD (IR780) imaging *in vivo*, we now present proofs-of-concept that the results differentiate between N-methyl-D-aspartate (NMDA) evoked neural activities in two distinct circuits with differential response profiles, i.e., sensorimotor cortex and hippocampus. Concurrent quantitative EEG (qEEG) recorded real time circuit dynamics. We hypothesized that NMDA evoked focal glutamate release in both circuits would correlate with increases of location-specific PA signals and time-specific EEG signals.

To test the hypothesis in hippocampus, we infused 0.3, 1, and 3 mM NMDA at 2 μl/min over 60 min via an implanted microdialysis probe. The dialysate samples collected every 20 minutes during the infusion were analyzed for focal changes in extracellular glutamate release and quantified by high-performance liquid chromatography (HPLC). Microdialysis at 0.3, 1, and 3 mM showed dose-dependent increases of glutamate (39%, 200% and 670 %, respectively) in hippocampus. We recorded dose-dependent increases of the PA signal with 0.3 and 3 mM NMDA infusion as predicted. Quantitative EEG at 3 mM NMDA infusion confirmed induction of focal seizure activity. Transcranial PA VSD imaging provided up to 301±42% of fractional neural activity index change measured at the contralateral side of the microdialysis probe with 3 mM NMDA infusion, compared to the decrease of -24±34% with 0.3 mM NMDA infusion. This graded response suggests dentate gyrus (DG) gatekeeping in hippocampus.

In sensorimotor cortex, intracerebral infusion of NMDA at 0.3 mM elicited the predicted increase of glutamate release, with a decrease of qEEG spectral power. . Transcranial PA VSD imaging had -13±37% of fractional neural activity index change during the 20 min of 0.3 mM NMDA infusion, consistent with surround suppression of depolarization as shown by qEEG of motor cortex.

We conclude that transcranial PA VSD imaging distinguished relatively greater cortical inhibition and threshold-level hippocampal focal seizure activity that both correlated with activities reported by qEEG signals. The results show this emerging technology to be an innovative and significant advance of functional neuroimaging.

1. Introduction

Whereas electrophysiological and invasive neurochemical techniques have been valuable in assessing activity within specific neural circuits in brain, there is a distinct need for a noninvasive means to image real-time regional functional activity *in vivo*. In particular, motor cortex and hippocampus are of interest, as they present distinct circuits with clear electrophysiological modulation of excitatory neurotransmission. It is long known that neocortical structures such as the motor cortex exhibit both excitatory and feedforward as well as feedback inhibitory mechanisms driven by NMDA that limit neural activity and modulate oscillatory firing. The focal application of low doses of NMDA is known to activate spreading cortical depression that depends on NMDA receptors (Hansen et al., 1980; Gjedde et al., 1981; Lauritzen et al., 1982; Marrannes et al., 1988). On the other hand, the hippocampal circuit has rows of excitatory pyramidal neurons all aligned in close proximity and similar orientation in the dentate gyrus (DG) with its hyperpolarized resting membrane potential that forms the putative gating for signals from adjacent cortices. Low amplitude excitatory inputs do not depolarize the DG neurons and therefore fail to open the DG gate (Andersen et al., 1966). Low amplitude excitatory signals are insufficient to bring the system to threshold for activation; however, with strong repetitive signals seizure activity can be induced. This is consistent with the hippocampus being the lowest seizure threshold region of the mammalian brain. This all-or-none gating system in the DG is therefore distinct in its circuit dynamics from the motor cortex.

Previous optical imaging approaches to local circuit inhibition (Petersen and Sakmann, 2001; Derdikman et al., 2003; Petersen et al., 2003) applied invasive procedures to overcome superficial imaging depth, and further extension to deeper brain regions such as the hippocampus was prohibitive. The imaging of electrophysiological or neurochemical dynamics within the hippocampus primarily has been accomplished by optical imaging of freshly-sliced brain tissue (Okubo et al., 2010) or magnetic resonance imaging spectroscopy (MRS) for non-invasive quantification of glutamate at high spatial resolution (Crescenzi et al., 2017; Voets et al., 2017). However, optical imaging and MRS suffer from the need to isolate brain tissue *ex vivo* and from slow imaging speed, respectively. The application of two-photon microscopy to measure calcium ion dynamics in specific deep brain structures, including hippocampus, has no temporal resolution in real-time. (Kondo et al., 2017) Therefore, non-invasive, real-time visualization with spatiotemporal resolution would be a significant advance, but such an approach would require neurochemical and electrophysiological characterization to validate the neural activity recorded by EEG.

Photoacoustic (PA) imaging is a hybrid approach combining optics and acoustics that provides a molecular signature to the neural activity assessed by acoustic transcranial imaging (Wang et al., 2003; Wang and Hu, 2012). PA imaging is based on thermo-elastic perturbation of a target evoked by light absorbance from a pulsed laser illumination, which generates radio-frequency (RF) acoustic pressure detected by piezoelectric ultrasound transduction or optical interferometry. With this unique imaging mechanism, several attractive applications have been proposed for preclinical and clinical research with tomographic and microscopic imaging modes, including detection of endogenous contrast of cancer indicators (e.g., melanoma (Zhang et al., 2006), breast microcalcifications (Kang et al., 2014; Kim et al., 2014; Kang et al., 2015)), monitoring of cancer angiogenesis (Yao et al., 2012), oxygen metabolism (Hu, 2016), and quantification of lipid content (Hui et al., 2017; Wu et al., 2017), among others.

Here, we validated *in vivo* transcranial PA neuroimaging of distinct neural circuit mechanisms activated by stimulation of N-methyl-D-aspartate (NMDA) receptors in motor cortex and hippocampus in rat brain *in vivo* through intact skull and scalp. This tri-modal neural sensing approach by means of microdialysis, quantitative electroencephalography (qEEG), and transcranial PA imaging simultaneously monitor neurochemical and electrophysiological changes in neural activity and associated glutamatergic

110 neurotransmission (Figure 1a). To stimulate these circuits, we infused NMDA by reverse microdialysis
111 that triggered localized changes of extracellular glutamate concentration (Drew et al., 2004) (Young and
112 Bradford, 1991). In the cortex, glutamate and γ- aminobutyric acid (GABA) mediate excitatory and
113 inhibitory synaptic events, respectively. NMDA receptor activation also facilitates the release of
114 neurotransmitter from synaptosomes prepared from terminals in the hippocampus and neocortices
115 (Sherman et al., 1991). We quantified the change of extracellular glutamate concentration evoked by
116 reverse microdialysis by direct microdialysis and high-performance liquid chromatography (HPLC). We
117 combined qEEG with microdialysis to evaluate the effect associated with surround inhibition in the
118 presence of glutamatergic excitation at motor cortex and hippocampus, respectively (Figure 1b).
119 Concurrently, the contrasting electrophysiological results were quantified and confirmed with transcranial
120 PA neuroimaging and qEEG recording (Figure 1c). Each of the three modalities thus provided
121 information with different degrees of specificity, including spatial and temporal specificity from PA
122 imaging, temporal specificity from qEEG, and focal neurochemical specificity from microdialysis in
123 target neural circuits, i.e., motor cortex and hippocampus.

124

125 2. Material and Methods

126 **Animal preparation.** For the proposed *in vivo* experiments, 8-9-week-old male Sprague Dawley rats
127 (Charles Rivers Laboratory, Inc., MA, United States) weighing 275-390g were used. The use of animals
128 for the proposed experimental protocol was approved by the Institutional Animal Care and Use
129 Committee of Johns Hopkins Medical Institute (RA16M225). Rats were housed in groups of 3 per cage
130 with free access to food and water, and maintained on a 12hr light / 12hr dark cycle.

131 **Fluorescence quenching-based near-infrared voltage-sensitive dye.** In the present *in vivo* study, we
132 used the fluorescence quenching-based near-infrared cyanine VSD, IR780 perchlorate (576409, Sigma-
133 Aldrich Co. LLC, MO, United States) as in our previous *in vivo* study differentiating a chemoconvulsant
134 seizure activity (Kang et al., 2017), and it have the analogous chemical structure of PAVSD800-2, our
135 new VSD validated in our previous *in vitro* study.(Zhang et al., 2017) This VSD yields fluorescence
136 emission leading to a reciprocal PA contrast with non-radiative relaxation of absorbed energy.

137 **Microdialysis.** On the day of the study the rats were weighed and anesthetized with urethane
138 (1.2mg/kg,). Urethane was given incrementally with alternating ip and sc dosing. Three (3) ml of isotonic
139 saline was given sc on each side of the body to keep the animal hydrated during the experimental
140 procedure. Body temperature was maintained until animal was fully anesthetized and ready for surgery.
141 For PA and EEG studies, an iv catheter was inserted into a tail vein prior to surgery for dye
142 administration during the studies. Once a stable plane of anesthesia was established, hair was shaved
143 from the scalp of each rat for improved optical/acoustic coupling for transcranial PA recording. The rat
144 was placed into a stereotaxic device (Stoeling Co. Wood Dale, IL). This fixation procedure was required
145 to prevent any unpredictable movement during PA or EEG recording of neural activities. A CMA12
146 microdialysis probe (Harvard Apparatus, Holliston, MA, USA) was implanted into either the right lobe
147 of the frontal cortex (stereotaxic coordinates: 1.5 mm lateral and 3.2 mm anterior to bregma, and 3 mm
148 below the surface of the dura) or the CA_3 region of the right hippocampus (stereotaxic coordinates:
149 3 mm lateral and 3.8 mm posterior to bregma, and 3.6 mm below the surface of the dura) (Paxinos and
150 Watson, 2014). The probe active exchange surface was 2 × 0.5 mm. For EEG and PA experiments,
151 probes were secured to the skull using dental acrylic cement.

152 ***In vivo* microdialysis**. *In vivo* microdialysis sampling was carried out as previously described (Baumann
153 et al., 2012; Elmore et al., 2017). For infusion experiments, NMDA (Sigma-Aldrich Chemicals, St. Louis,

154 Mo) was weighed, solubilized, and diluted to the desired concentration in artificial cerebrospinal fluid
155 (NaCl, 147 mmol/L; KCl, 2.7 mmol/L; $CaCl_2$, 1.2 mmol/L; $MgCl_2$, 0.85 mmol/L)(Harvard Apparatus,
156 Holliston, MA, USA) on the study day. Once the probe was inserted and secured, it was perfused with
157 artificial cerebrospinal fluid pumped at a flow rate of 2 μl/min. Samples were collected at 20 min
158 intervals, and immediately transferred to a -80 °C freezer until assayed. To allow sufficient time for the
159 glutamate levels to equilibrate, three baseline samples were collected an hour following initiation of
160 infusion. Following these samples, NMDA was infused into the brain directly through the dialysis probe
161 with the same pump parameters as used for the baseline samples. Dialysate samples were assayed for
162 glutamate by a two-step process using HPLC-ECD on an Eicom HTEC-500 system (EICOM, San
163 Diego, CA, USA). After passing the samples through a separation column, they were processed via a
164 column containing immobilized L-glutamate oxidase enzyme, resulting in the release of hydrogen
165 peroxide. The hydrogen peroxide concentration was then determined using a platinum working
166 electrode. Chromatographic data were acquired online and exported to an Envision software system
167 (EICOM, San Diego, CA, USA) for peak amplification, integration, and analysis.

168 **Quantitative EEG.** All EEG recordings utilized a three-electrode paradigm: 1 recording, 1 reference
169 (aligned to the site of activation) and 1 ground over the rostrum. The electrodes (IVES EEG; Model #
170 SWE-L25 – IVES EEG solutions, MA, USA) were fixed with minimal cyanoacrylate adhesive
171 (KrazyGlue), similar to previous protocols (Airan et al., 2017). Data acquisition was performed using
172 Sirenia software (Pinnacle Technologies Inc., Kansas, USA) with synchronous video capture. Data
173 acquisition had a 14-bit resolution, 400Hz sampling rate, and a band pass filter between 0.5 Hz and 60
174 Hz. The acquisition files were stored in an .EDF format and scored manually, using real time annotations
175 from the experiments. EEG power for 2-second epochs was done using an automated fast Fourier
176 transformation module in Sirenia software (Kang et al., 2018).

177 **Photoacoustic imaging.** We used real-time PA data acquisition to record electrophysiological neural
178 activities *in vivo*: an ultrasound research system consisted of an ultrasound linear array transducer (L14-
179 5/38) connected to a real-time data acquisition system (SonixDAQ, Ultrasonix Medical Corp., Canada).
180 The center frequency of the transducer was 7.1 MHz to obtain good sensing depth for neural activities in
181 deep brain tissue. To induce the PA signals, pulsed laser light was generated by a second-harmonic (532
182 nm) Nd:YAG laser pumping an optical parametric oscillator (OPO) system (Phocus Inline, Opotek Inc.,
183 USA), providing 690-900 nm of tunable wavelength range and 20 Hz of the maximum pulse repetition
184 frequency. A bifurcated fiber optic bundle, each 40 mm long and 0.88 mm wide, was used for laser pulse
185 delivery. The PA probe was posed between the outlets of the bifurcated fiber optic bundles using a
186 customized, 3-D printed shell for evenly distributed laser energy density in the lateral direction on rat
187 scalp surface. The alignment of outlets was focused specifically at 20 mm depth. The PA probe was
188 positioned in the sagittal plane to cover the barrel cortex and hippocampus at the same time. Lateral
189 position of the probe was at the contra-lateral side of microdialysis probe: 1.5 mm for motor cortex
190 recording; 3 mm for hippocampus. The distance between the PA probe and the rat skin surface was 20
191 mm filled with acoustic gel, and the resultant energy density was at ~5 mJ/cm^2 , which is far below the
192 maximum permissible exposure (MPE) of skin to laser radiation by the ANSI safety standards. (Anon,
193 1975) A wavelength of 790 nm was used, at which sufficient absorbance can be obtained by the near-
194 infrared VSD, i.e., IR780 perchlorate. Also, probing at the wavelength prevented the undesired time-
195 variant change of oxygen saturation, being at the isosbestic point of Hb and HbO_2 absorption spectra.
196 Fig. 4b presents a representative sagittal cross-sectional PA image of a rat brain. The brain outline was
197 drawn based on the rat brain atlas (Paxinos and Watson, 2014). Detailed information of neural activity
198 reconstruction using normalized time-frequency analysis can be found in our previous publication (Kang
199 et al., 2017).

***In vivo* experimental protocol.** The *in vivo* protocols were designed for simultaneous multi-modal sensing of the neural activity at motor cortex and hippocampus: microdialysis-qEEG and microdialysis-PA imaging. Figure 2 shows a detailed schematic protocol for each group representing the response to the administration of NMDA, Lexiscan and VSD (i.e., IR780 perchlorate). PA and qEEG data acquisition was performed for 40 min to correlate with three microdialysis samples collected at 20-min intervals. VSD and Lexiscan followed the data acquisition sequence with 3-min delay, thereby 5 min of baseline phase was guaranteed for neural activity index reconstruction in PA imaging before starting NMDA infusion. The dosing protocol for Lexiscan and VSD administration was as follows: through an iv tail vein catheter, 150 μl of Lexiscan (0.4mg/5ml) was injected, followed by 200 μl of VSD at 2mg/ml concentration, flushed immediately with 150 μl of 0.9% isotonic saline. The EEG signal at motor cortex was recorded an identical preparation procedure as the PA imaging, including animal preparation and administration of IR780, Lexiscan and experimental duration time for all recordings.

Brain histology. Rats used for the above protocol were sacrificed, and whole brains immediately harvested and placed in 10% formalin. All brains were allowed to fix in fresh 10% formalin for at least 48 hours with gentle agitation on a conical rotator. Subsequently, the brains were processed through a series of sucrose gradients (15%, 20%, 30% for 12-24 hours each) for cryoprotection. Brains were sectioned frozen at 300 μm thickness. Tissue sections were mounted on slides in ProLong Diamond Anti-face mountant. Slides with sections were imaged using an Olympus OM-D E-M5 Mark II for bright field image and using LI-COR Odyssey for fluorescence visualization.

3. Results

NMDA-evoked glutamatergic neurotransmission. Intracortical and intrahipocampal infusion of NMDA diluted into artificial cerebrospinal fluid at the required concentrations, was infused through the microdialysis probe. Concentrations of glutamate release in the dialysate were calculated from values of three baseline samples collected at 20 minutes intervals before NMDA infusion. During infusion, samples continued to be collected every 20 minutes for the remainder of the study. Glutamate release were calculated as a % of basal values. Figure 3 shows the effect of NMDA infusion on glutamate release in the motor cortex and the hippocampus of anesthetized rats. Figure 3a shows that infusion of 0.3 mM NMDA into the motor cortex caused a roughly 60 % increase in glutamate levels as compared to baseline samples. The increase occurred in the first 20-minute sample collection period following the onset of NMDA infusion, and was sustained for the full infusion period. Figure 3b demonstrates the dose-related response of NMDA infusion at 0.3, 1.0, and 3.0 mM into the hippocampus, where 0.3 mM NMDA caused a roughly 40% increase in glutamate levels that remained elevated for the duration of the infusion; the 1.0-mM NMDA infusion appears to cause doubling of the glutamate levels in the hippocampus compared to baseline. This increase observed at the 1.0-mM remained elevated through to the end of the NMDA infusion. However, at 3.0-mM, the NMDA infusion raised the glutamate level roughly 6-fold, above baseline level, which peaked during the second 20-minute sampling period, after which it began a steady decline to the termination of the infusion. The increase in glutamate release seen in microdialysis in the motor cortex did not correlates with measures of VSD imaging with PA, but good correlations were seen in the hippocampus. Interestingly, qEEG also revealed no seizure activity with infusion into motor cortex at the 0.3-mM concentration, but elicited a strong seizure response in hippocampus with infusion of 3-mM NMDA in the time period that coincided with peak glutamate activity in the dialysate.

EEG of electrophysiological activity in motor cortex and hippocampus. We used qEEG to investigate whether the NMDA-induced glutamate release seen with microdialysis activates circuits in

245 motor cortex and hippocampus. In order to establish circuit activity differences of reactivity to the
246 specific focal stimulations, recordings of qEEG were used to interpret PA values acquired with the same
247 protocols to establish spatial and temporal relationship. The temporal specificity of qEEG expressed
248 circuit responses in realtime, before and after focal NMDA infusion. However, qEEG lacks spatial
249 resolution, and records cannot be obtained from deep brain structures with leads placed on brain or skull
250 surfaces. Therefore, we opted not to place in-depth electrodes, in order to maintain the experiments as
251 possible. We made the stimulation focal, according to the previous proof-of-concept results by PA
252 detection onset of generalized seizures through an intact skull (Kang et al., 2017).

253 When 0.3-3 mM NMDA was delivered to distinct motor cortex and hippocampal circuits by
254 microdialysis probe (Figure 1a) (Paxinos and Watson, 2014), results showed that NMDA infusion of 0.3
255 mM NMDA at the M2 coordinates of the motor cortex caused the expected rise of local glutamate
256 release measured in microdialysis (Figure 3) that had an effect on qEEG spectral power; specifically in
257 the gamma frequency (Figure 4-a2). The resulting qEEG suppression seem to indicate focal glutamate-
258 induced activation of surround inhibition; becoming more prominent over the duration of the infusion
259 (Figure 4-b2). In contrast, a 3 mM infusion into the hippocampus immediately resulted in increased
260 bursts of gamma power in the EEG, followed by a focal seizure (Figure 4 and S1). Unlike the cortical
261 circuit that showed increasing EEG suppression over time, the hippocampal circuit continued to exhibit
262 short epileptiform discharges throughout the NMDA infusion period (Figure S1b V), indicating
263 continued disruption of the DG gating during the entire duration of the NMDA infusion.

264 **Transcranial PA imaging.** Transcranial PA neuroimaging of distinct neural mechanisms in motor
265 cortex and hippocampus was performed at the contralateral position of microdialysis probe (Figure 5a).
266 The PA sagittal planes obtained at 790 nm presented a sufficient sensitivity at the depths of interest in rat
267 forebrain: 2.5 mm and 3.6 mm for motor cortex and hippocampus, respectively (Figure 5b). The motor
268 cortex imaging plane presented high intensity at the superior sagittal sinus at superficial depth, and the
269 morphological boundary of brain tissue could be distinguished based on the rat brain atlas and PA signal
270 distribution representing both blood and VSD in brains. The sagittal PA imaging plane of hippocampus
271 also revealed the cross-sections of transverse sinus and inferior cerebral vein in the superficial depth
272 range, but it also shows sufficient sensitivity at the depth of hippocampus. From the regions-of-interest
273 (ROIs) indicated with solid white box, time-averaged neural activity index was reconstructed pixel-by-
274 pixel for baseline (5 – 10 min) followed by the results for time bins in 10 min interval: 10 – 20 min, 20 –
275 30 min, and 30 – 40 min (Figure 5c). As a result, the substantial amount of circuit dynamics was detected
276 at hippocampus with 3 mM NMDA infusion, while demonstrating negligible change at motor cortex as
277 predicted by their distinct mechanisms. Otherwise, the hippocampus with 0.3 mM NMDA infusion did
278 not present any significant change, which implies a failure to overcome high activation threshold of DG
279 gatekeeping with 0.3 mM NMDA infusion. This interpretation is supported with the subtle change in
280 extracellular glutamate concentration shown with forward microdialysis (Figure 3b)

281 To further characterize the PA VSD intensity change, the normalized neural activity index
282 sequence at the ROIs indicated by red dots was plotted as a function of the corresponding normalized
283 PA intensity (Figure 5d). Note that the size of each ROI was 1 x 1 mm^2, and the reference intensity was
284 obtained from the baseline phase: 5-10 min. In motor cortex, 0.3-mM NMDA infusion presented
285 complex suppression mechanism in the cortical region: The quantification of normalized neural activity
286 index presented 1.00 ± 0.36, 0.87 ± 0.37, and 1.19 ± 0.36 for baseline (5 – 10 min), and first (10 – 30
287 min) and second (30 – 40 min) microdialysis phases (NMDA1 and NMDA2), respectively. This result
288 suggests the initial suppression at the first 20 min of NMDA infusion (i.e., -13 %), which is well
289 correlated to the electrophysiological validation in qEEG recording (Figure 4-a2). On the other hand, 3-
290 mM NMDA infusion at hippocampus yielded significant elevation of neural activity index as
291 corresponding PA intensity decreases: 1.00 ± 0.35 %, 1.55 ± 0.36 %, and 1.74 ± 0.33 % of normalized

292 neural activity indices for baseline, NMDA1, and NMDA2 phases, respectively. This validates the
293 proposed VSD mechanism which yields suppressive intensity to neuronal depolarization (Zhang et al.,
294 2017). Otherwise, focal 0.3 mM NMDA infusion at hippocampus did not presented any statistically-
295 significant circuit activity increase compared to the baseline neural activity index: 1.00 ± 0.31 %, 0.99 ±
296 0.41 %, and 0.76 ± 0.34 % of normalized neural activity indices for baseline, NMDA1, and NMDA2
297 phases, respectively. These results support our hypothesis that PA imaging can differentiate the DG
298 gating function at the hippocampus. In all, when tracing the change of circuit dynamics from the
299 baselines, the 3-mM NMDA infusion at hippocampus presented statistically significant difference
300 compared to those with 0.3 mM at both hippocampus and motor cortex ($P < 0.0001$). The VSD
301 mechanism suppressive to neuronal depolarization could be also confirmed with the temporal specificity
302 of PA neuroimaging. The successful extraction of neural activity index was also confirmed in Figure 5e
303 which presents the normalized neural activity index (top panel) and relative PA intensity to baseband
304 frequency component (bottom panel). As shown in the figure, NMDA inset produces suppressive PA
305 intensity around 1-dB from basal level, which is also synchronized to the focal seizure presented in
306 qEEG given by DG gating breakdown (Figure 4-b2 and Figure S1 V), leading to 2.5-times instantaneous
307 increase of neural activity index for around 20 sec. Refer Figure S2 for the entire neural activity index and
308 PA intensity traces.

309 Figure 6 presents the normalized neural activity index as a function of extracellular glutamate
310 concentration at motor cortex and hippocampus. The motor cortex presents the comparable amount of
311 neural activity index with that of baseline phase at hippocampus (n = 1), but 3 mM NMDA infusion into
312 hippocampus produced exponential increase in neural activity index when the extracellular glutamate
313 concentration exceeds 6 μM in microdialysis sampling (n = 2). These results again confirm the DG
314 breakdown with specific glutamatergic potential threshold at neural circuitry.

315 **Brain histology.** Brain tissue was extracted after all *in vivo* experimental protocols. The brain was frozen-
316 sectioned *into* 300-μm thickness slices and evaluated to confirm probe placement using the hemorrhage
317 caused by the microdialysis probe insertion for the NMDA infusion and collections as a marker. Figure 6
318 shows the bright-field images of the coronal plane of the motor cortex and hippocampus at 3.2 mm and
319 -3.8 mm from bregma, respectively. White arrows indicate the hemorrhage caused by the microdialysis
320 probe positioned at the following coordinates: bregma 3.2 mm, lateral 1.5 mm, depth 2.5 mm for motor
321 cortex; bregma -3.8 mm, lateral 3 mm, and depth 3.6 mm for hippocampus. The VSD staining of brain
322 tissue was confirmed with near-infrared fluorescence microscopy. Uniform VSD fluorescence was found
323 in the VSD perfusion group, while negative control (VSD -) presented negligible fluorescence emission
324 (Figure S3), which confirms the results in our previous publication (Kang et al., 2017).

325

326 # 4. Discussion

327 The application of PA imaging was expanded to neuroscience (Nie et al., 2012; Liu et al., 2017; Li
328 et al., 2018) as label-free transcranial PA imaging of neurovascular coupling proposed as a means to
329 quantify hemodynamic changes (Hu and Wang, 2010; Zhang et al., 2018). However, this approach does
330 not yield quantitative neural activities that directly correspond to electrical activity, as required for the
331 proposed imaging of distinct neural mechanisms within motor cortex and hippocampus. Hemoglobin
332 provides an effective contrast signal, and there has been extensive investigations into more effective
333 exogenous contrast agents (Luke et al., 2011; Huynh et al., 2014; Moon et al., 2015; Ju et al., 2016; Weber
334 et al., 2016). Several PA approaches detect electrophysiological neural activities with functional voltage
335 sensors. Deán-Ben et al. showed real-time PA tomography of a genetically encoded calcium indicator,
336 GCaMP5G, using zebrafish *in vivo* (Deán-Ben et al., 2016). Sheryl Roberts, et al. also proposed a new

337 metallochromic calcium sensor for PA imaging (CaSPA) which has a high extinction coefficient, a low
338 quantum yield, and high photo-bleaching resistance for brain and heart imaging (Roberts et al., 2018).
339 Ruo et al. reported PA imaging of neural activity evoked by electrical stimulation and 4-aminopyridine-
340 induced epileptic seizures using hydrophobic anions such as dipicrylamine (DPA) in mouse brain.(Rao et
341 al., 2017) However, these voltage sensors requires PA imaging at the visible spectral range (488 nm and
342 530 nm for GCaMP5G; 550 nm for CaSPA; 500 nm and 570 nm for DPA), which is suboptimal for the
343 proposed study when especially imaging hippocampus posed at 5 mm – 8 mm including intact scalp and
344 cortex for the rat (Nowak et al., 2011; Paxinos and Watson, 2014). Recently, we proposed transcranial
345 PA recordings of brain activity *in vivo* with a near-infrared voltage-sensitive dye (VSD, 790 nm), delivered
346 through the blood-brain barrier (BBB) via pharmacological modulation, as a promising tool to transcend
347 current functional neuroimaging limitations, particularly as it relates to sensing depth (Kang et al., 2017;
348 Zhang et al., 2017). The studies demonstrated that transcranial PA imaging of near-infrared VSD
349 distinguishes *in vivo* seizure activity in stimulated rat brains from that of control groups in real time (Kang
350 et al., 2017). However, the results were limited by the use of a global chemoconvulsant, causing
351 perturbation across the entire brain caused by the intraperitoneal administration of penetylenetetrazole
352 (PTZ). In this paper, we presents further advances in PA VSD imaging focal neural stimulation of
353 heterogeneous neural circuits, with concomitant validations from qEEG and glutamate quantification
354 using microdialysis, respectively.

355 The set of experiments described here yield key findings as follows: (1) The microdialysis-
356 dependent NMDA infusion into the central nervous system (CNS) lead to a reliable increase in focal
357 extracellular glutamate concentrations in both the cortex and hippocampus. (2) Unlike the microdialysis
358 glutamate release for both cortex and hippocampus, transcranial PA imaging and qEEG showed distinct
359 phenotypes in the cortex vs. hippocampus. There was a fall in electrophysiological responses in the
360 motor cortex indicating NMDA receptor activation in the motor cortex circuit lead to strong activation
361 of local inhibitory circuits either directly or as a consequence of activation of feedback circuits (Sachdev
362 et al., 2012). In contrast, NMDA activation in the hippocampus triggers an all-or-none type of circuit
363 dynamics that lead to the initiation of a focal seizure in the hippocampal circuit. (3) Transcranial PA
364 neuroimaging data successfully validated these EEG specific opposite circuit activity profiles for the
365 similar focal activation of NMDA receptors. No circuit activity was detected in the motor cortex on the
366 PA imaging despite an increase in focal glutamate levels recorded in the same rats. In contrast, the PA
367 signal yielded hot spots of neuronal activity following NMDA receptor activation in the hippocampus.

368 These results allow us to reassess the differential neural mechanisms modulating activity between
369 motor cortex and hippocampus as described in the Introduction: Strong local circuit inhibition has been
370 observed with transcranial PA neuroimaging and qEEG recording. Cortical inhibition may be due to
371 suppression of neuronal firing mediated by γ-amino butyric acid (GABA) receptors (Krnjević, 1997)
372 secondary to activation of GABAergic inhibitory interneurons by NMDA (Homayoun and Moghaddam,
373 2007). Slice electrophysiology in animal and human cortical tissue have revealed two main phases of
374 inhibition following stimulation; a "fast" phase mediated by ionotropic $GABA_A$ receptors and a "slow"
375 phase mediated by metabotropic $GABA_B$ receptors (Connors et al., 1988; McCormick, 1989). Inhibition
376 provides the ability to locally modulate excitation as well as gate rhythmic activity, which is critical for
377 proper sensorimotor inputs and outputs. Such findings likely indicate a general pattern of cellular
378 connectivity intrinsic to cortical organization.

379 On the other hand, the hippocampal circuitry provides a second distinct circuit that contrasts
380 with that of the motor cortex to assess PA specificity, as it reveals the proportional excitation of
381 glutamatergic neurotransmission. The DG of the hippocampus is positioned as a gatekeeper for the
382 canonical trisynaptic circuit, regulating the vast cortical inputs that regulate the limbic system.
383 Characteristically, the DG displays a high activation threshold; a trait that is associated with executing

384 cognitive functions that require pattern separation and completion (Chawla et al., 2005). The ability to
385 differentiate inputs, and diversify cognitive functions, is mediated by inhibition. Suitably, the DG is
386 profusely innervated with strong GABAergic inhibition (Szabo et al., 2017). In diseases of
387 hyperexcitability, such as epilepsy, the DG can regulate pathological seizure activity from invading the
388 limbic system. This gating is evident in recordings from the DG during low frequency stimulation of the
389 perforant path fibers. The DG displays the ability to selectively filter low frequency stimulation by
390 subsequent activation of strong inhibitory post synaptic potentials (Andersen et al., 1966). Yet, longer or
391 higher frequency stimulations resulted in excitatory post synaptic potentials generated by the DG. This
392 disruption of DG gating has been clearly demonstrated by utilizing VSD imaging techniques, reinforcing
393 DG's role of gatekeeping (Ang et al., 2006). The consequence of gatekeeping is that in epilepsy the DG
394 generates and propagates seizure activity.

395 Further investigations are required to advance our current perspectives available with tri-modal
396 sensing, including PA, qEEG, and microdialysis. Previous studies have shown that application of
397 glutamate to the hippocampal pyramidal neurons produces a fast-rising brief depolarization (Taube and
398 Schwartzkroin, 1987). Therefore, the use of PA will enable us to more precisely assess glutamate and
399 GABA dynamics in order to formulate a more complete profile of circuit activation. Once homeostasis is
400 disrupted, neuronal activity is sensitive to changes both of excitatory and inhibitory mechanisms. . Faster
401 neurochemical recording is another approach that may prove useful in assessing the impact of these
402 measures. Although microdialysis successfully provided quantitative, focal neurochemical
403 concentrations, the sampling rate of 1 sample per 20 min was slow. Techniques offering faster temporal
404 resolution may allow more meaningful comparison of the neurochemical changes yielded by
405 microdialysis and the electrophysiological events monitored by qEEG and PA imaging. One such
406 technique, using custom built hardware and the Amplex Red method, achieved fluorescence-based
407 quantification of glutamate from samples taken every 5 seconds, though reliability appeared to be limited
408 when higher glutamate concentrations were measured (Medina-Ceja et al., 2015). Implantable glutamate
409 biosensors allow sub-second readouts of neurochemical concentrations. However, current limitations
410 include sensitivity, selectivity, and high cost; recent developments in materials, effective modeling, and
411 sensor design may soon alleviate some of these limitations (Clay and Monbouquette, 2018; Moon et al.,
412 2018).

413 EEG records the voltage differentials occurring between the reference and recording electrode
414 representing underlying circuit activity with high temporal specificity. Hypersynchronous neuronal
415 activity in any given circuit results in high amplitude high frequency activity in the EEG, causing the
416 generation of potent local excitatory events. In contrast, interneurons known to fire action potentials at
417 very high frequencies inhibit neuronal circuit activity efficiently because a single interneuron can
418 innervate and inhibit a large population of pyramidal neurons simultaneously. Depending on the circuit,
419 simultaneous interneuron activation can be followed by a rebound depolarization due to simultaneous
420 disinhibition of the excitatory neurons innervated by this interneuron population.

421 Based on the validated circuit activity measured via transcranial PA imaging and qEEG
422 successfully differentiated the circuit activity between these regions with spatial and temporal specificity.
423 However, future developments should serve to further advance the efficacy of PA imaging in
424 neuroscience. (1) We expect that improved signal processing for extracting neural activity from the
425 ubiquitous blood context will enable better characterization of brain function. The present in vivo
426 experiments confirmed the possibility of background suppression. Enhanced signal processing and/or
427 use of multi-spectral wavelengths may allow significantly improved spectral differentiation of
428 electrophysiological activities in the brain, leading to development of novel quantitative metrics for real-
429 time brain activity measures. Having isotropic resolution with 2-D PA probe would be also an interesting
430 direction to pursue as follow up to the present work. The use of 2-D PA probe would not only allow

real-time volumetric information, but also enable the suppression of off-axis interference. Even though we presented that neural activity can be successfully discerned with current 1-D PA probe, its sensitivity might be affected by off-axis interferences especially from the elevation direction because of the limited acoustic lens focusing at a fixed depth. The neuroimaging using 2-D PA probe would reject those interferences by the advanced electrical beamforming capability in axial, lateral, and elevation directions.

In all, the EEG results indicate that NMDA infusion and the associated increase in focal glutamate had opposite physiological results in the two circuits: NMDA triggers glutamate release that excites the neural circuit, but it is nearly immediately blocked by surround inhibition at motor cortex or causes runaway excitation in the hippocampus by overcoming DG gating. This is reflected in the lower seizure threshold of the hippocampus compared to neocortex. This suggests that the activations of NMDA receptors can modulate neural circuits into diametrically opposite responses *in vivo*. Transcranial PA imaging demonstrated its ability to differentiate the changes in electrophysiology found in these circuits, and its findings were validated with qEEG. PA imaging is a promising technology for the imaging of neural events in real time.

Author Contributions

DFW, AAG and MB originally conceived of the NMDA administration and of microdialysis with PA idea and helped to design the overall research plan. DFW critically revised the focus of the results and final version and interpretation. LML SDK helped to design the overall research plan, helped plan specific experiments and all contributed to the review and writing of the manuscript. Jeeun K, SDK, JSE, BJS, HV planned and carried out in vivo experiments, analysed the research outcomes, and wrote key elements of the first draft of the manuscript. Jeeun K analysed and interpreted with EB the PA measurements, HV and JE the NMDA dosing design and microdialysis and SDK and BS the EEG experiments HV and LML devised the VSD vehicle preparation. APM performed histopathological analysis. - MH planned and supervised confirmation of VSD penetration into brain tissue also contributed to the final version of the manuscript. AG critically revised experimental design, draft, and final versions of manuscript, and interpretation of results. Jin K developed, funded, and participated in the current PA system design. AR participated in early planning and critically read and edited the manuscript. He has contributed both technically and materially to support this research. EB led the development, system specification, design specification, and funding of the current photoacoustic system. Secured the funding of the needed imaging experiments throughout the life time of the project, including taking responsibility of 3 full-time research members specifically for this work, JK and AM. Further, he has contributed intellectually by mentoring these members and providing input on manuscripts, and participating on PI meetings. DFW, AR and AG provided the original funding for the in vivo experiments MB provided resources and personnel and vital collaboration for the microdialysis part of the experiment.

Funding

This work was supported by the NIH Brain Initiative under Grant No. R24 MH106083-03 (DFW, AR, AG, EB AG HV, JE) and the NIH National Institute of Biomedical Imaging and Bioengineering under Grant No. R01EB01963. NIH National Institute of Child Health and Human Development (NICHD) for R01HD090884 (SDK). NIH National Institute of Heart, Lung and Blood (NHLBI) under grant number R01HL139543. National Cancer Institute (NCI) under grant number R21CA202199 and its equipment supplement. Funding of the PA equipment via resources of Jin K and EB NSF Career award #1653322

Conflict of Interest Statement

The authors declare that the research was conducted in the absence of any commercial or financial relationships that could be construed as a potential conflict of interest.

481 **Figures**

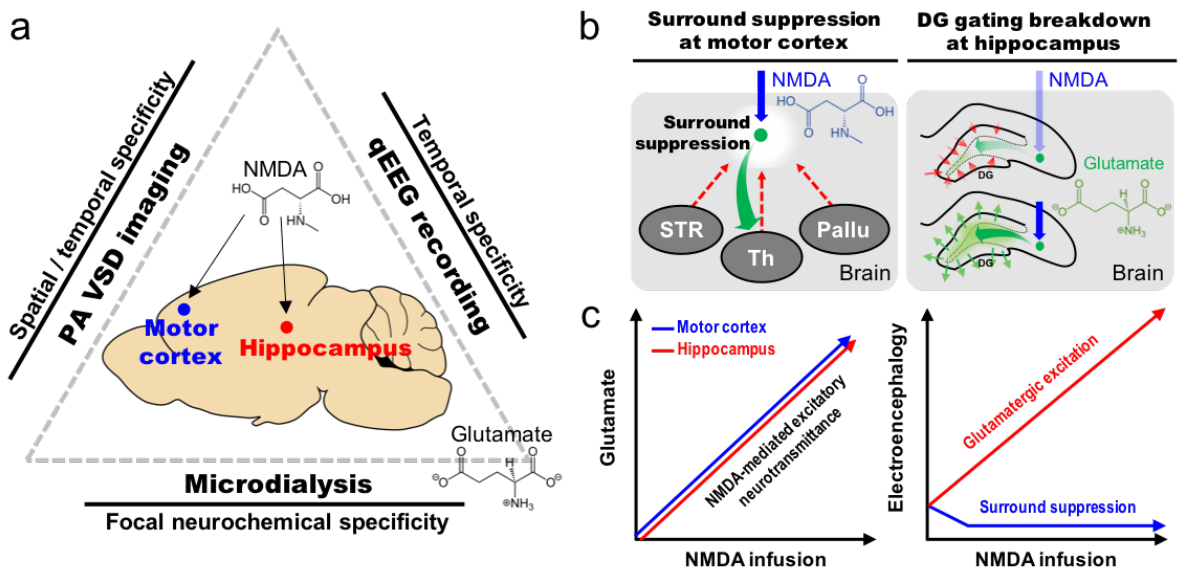

482

483 **Figure 1 Tri-modal sensing of distinct changes in electrophysiology at motor cortex and hippocampus.**
484 (**a**) Tri-modal neural sensing approach. (**b**) Surround suppression at motor cortex and dentate gyrus (DG) gating
485 breakdown at hippocampus to a focal NMDA infusion. (**c**) Diversion of an electroencephalogy for NMDA-
486 mediated glutamatergic neurotransmissions. NMDA, N-methyl-d-aspartate; STR, subthalamic nucleus; Th,
487 Thalamus; Pallu, Pallidus.

488

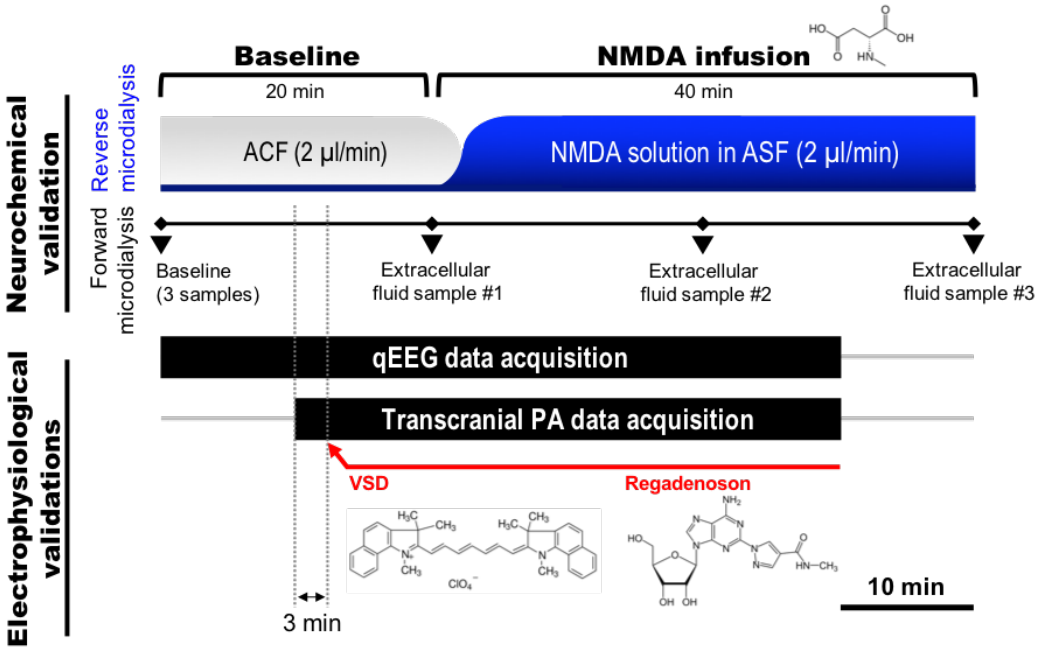

489

490 **Figure 2 *In vivo* experimental protocol.** Tri-modal sensing of distinct mechanisms at motor cortex and
491 hippocampus using forward microdialysis, PA imaging, and qEEG. ACF, artificial cerebrospinal fluid.

492

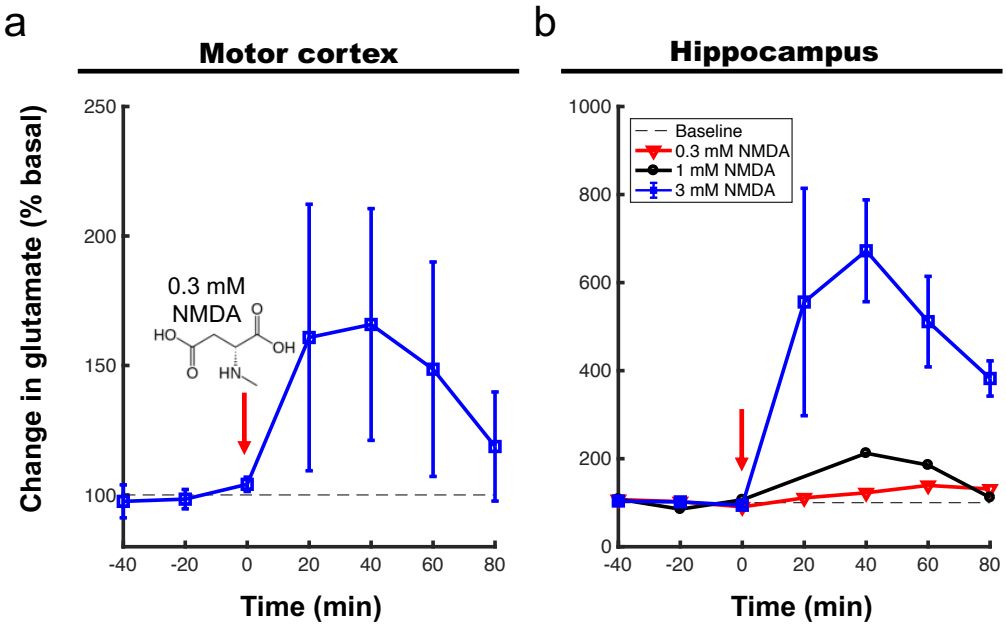

493

494 **Figure 3. The effects of NMDA infusion on extraceullular glutamate concentrations in anesthetized rats,**
495 **as compared to % baseline.** (**a**) 0.3 mM NMDA infusion into the motor cortex causes the glutamate to increase,
496 culminating in a 65% increase as compared to % baseline. (**b**) 0.3, 1.0, and 3.0 mM NMDA infusion into the
497 hippocampus caused maximal glutamate increases of 39%, 112%, and 572% respectively as compared to %
498 baseline.

499

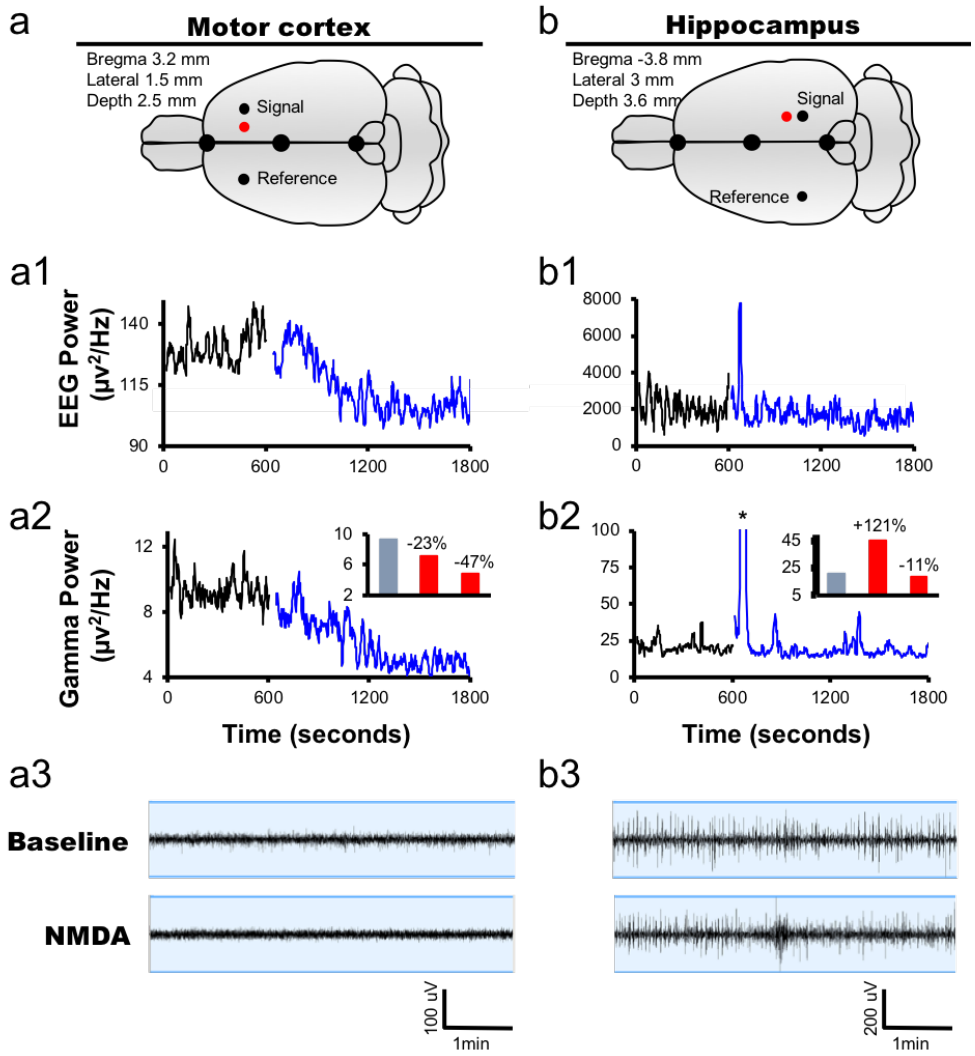

Figure 4. qEEG of motor cortex and hippocampus circuit dynamics following focal NMDA infusion. (**a**) Illustrates stereotaxic coordinates for the microdialysis probe and recording leads for the motor cortex. Ground electrode was implanted over the rostrum for both locations. Full EEG power (**a1**) shows a 10-minute baseline recording (blue trace), followed by two consecutive 10 min traces (red traces) of focal NMDA infusion. Overall EEG showed a drop in power after onset of focal NMDA infusion. (**a2**) Respective gamma power with baseline (blue trace) and focal NMDA infusion (red trace); power drop in gamma over the NMDA infusion period (first 10-minutes 23% decrease, second 10-minute 47% decrease when compared to baseline; see inset). (**a3**) Five minute raw EEG traces, blue lines indicate +/- 200uV, (attenuation of EEG waveforms seen with NMDA). (**b**) Illustrates stereotaxic coordinates for the microdialysis probe and recording leads for the hippocampus. Full EEG power (**b1**) shows a 10-minute baseline recording (blue trace), followed by two consecutive 10 min traces (red) of focal NMDA infusion. In contrast to the motor cortex, hippocampal EEG demonstrated onset of epileptiform discharges. (**b2**) Respective gamma power trace for hippocampal recordings demonstrates a 121% increase in gamma in the first ten minutes, and an 11% decrease in the second ten minutes, when compared to baseline (see inset). (**b3**) Five-minute raw EEG traces of the hippocampus, blue lines indicate +/- 200uV, NMDA infusion increased epileptiform activity, seizure indicated by asterisk in b2. For expanded time scales of hippocampal seizure see Supplemental 1.

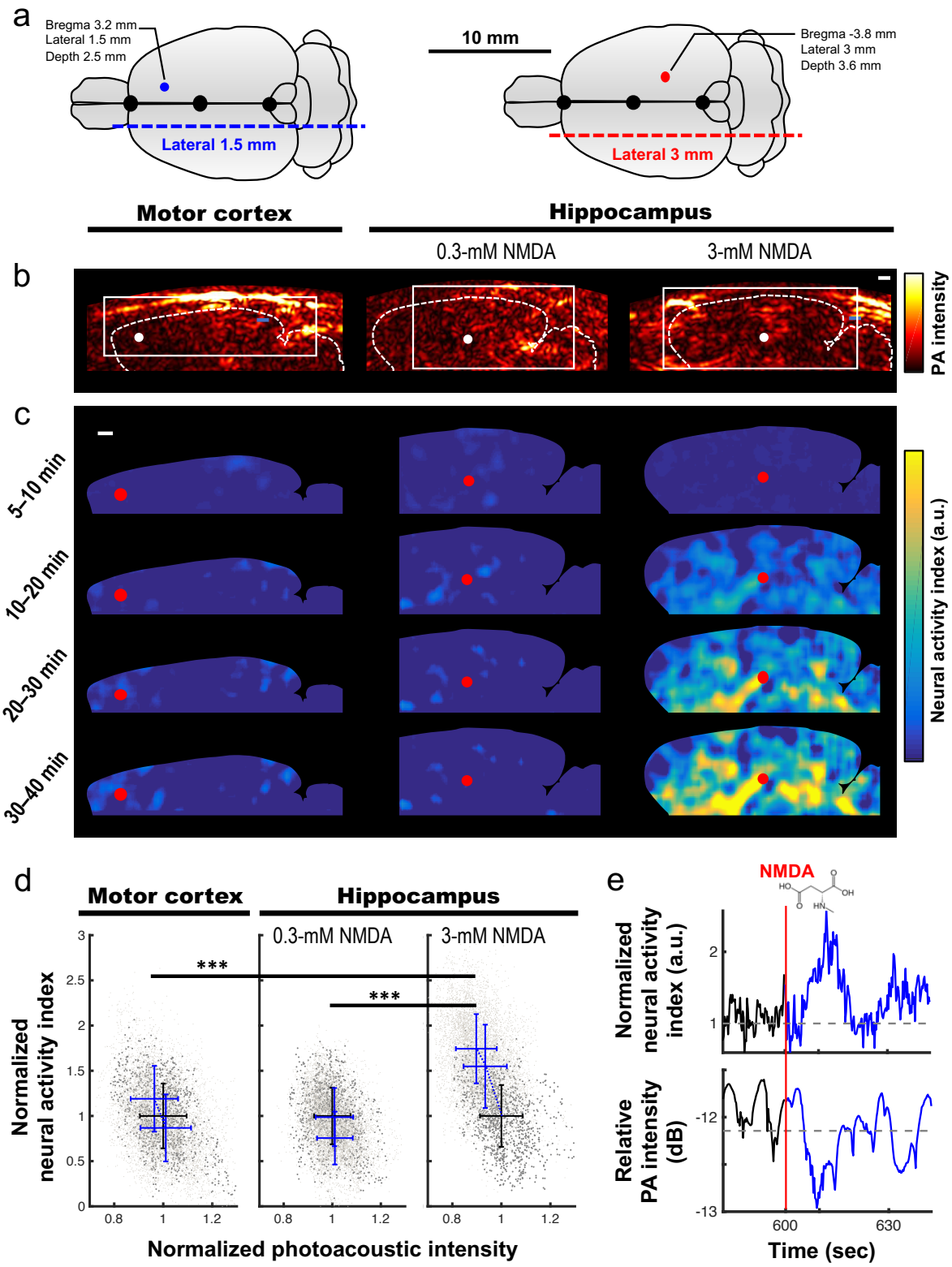

Figure 5. Transcranial PA neuroimaging of the distinct circuit dynamics at motor cortex and hippocampus following focal NMDA infusion. (**a**) Illustration of stereotaxic coordinates for the microdialysis probe and sagittal cross-sections for real-time PA recording. The sagittal PA imaging plane was selected in the contralateral side of the microdialysis probe infusing NMDA into the brain – motor cortex and hippocampus were recorded at 1.5 mm and 3 mm of lateral positions, respectively. (**b**) Sagittal

525 PA cross-sections at 790 nm and (**c**) time-averaged neural activity maps at each time points: 5-10 min;
526 10-20 min; 20-30 min; 30-40 min. Note that the points in (**b**) and (**c**) indicate microdialysis probe in
527 contra-lateral positions. Dotted line indicates the boundary of sagittal section derived from the rat brain
528 atlas and scaled accordingly (Paxinos and Watson, 2014), and dotted rectangular indicators are the
529 regions for temporal-frequency analysis reconstruction. (**d**) Normalized neural activity indices as a
530 function of corresponding normalized PA intensities. Black lines: baseline; blue lines: first and second
531 NMDA infusion phases. Dotted blue line indicates the progression of the correlation between the
532 normalized neural activity indices and PA intensities. Gray dots in the background represent the
533 distributions of individual data points: bold gray, data points in baseline; light gray, data points with
534 NMDA infusion. (**e**) Instantaneous suppression of PA intensity at the onset of NMDA infusion, which
535 also presented with qEEG in Figure 4-b2, leading to the high-intensity neural activity index trace. Gray
536 dotted lines indicate the basal level measured during baseline phase, i.e., 5 – 10 min.

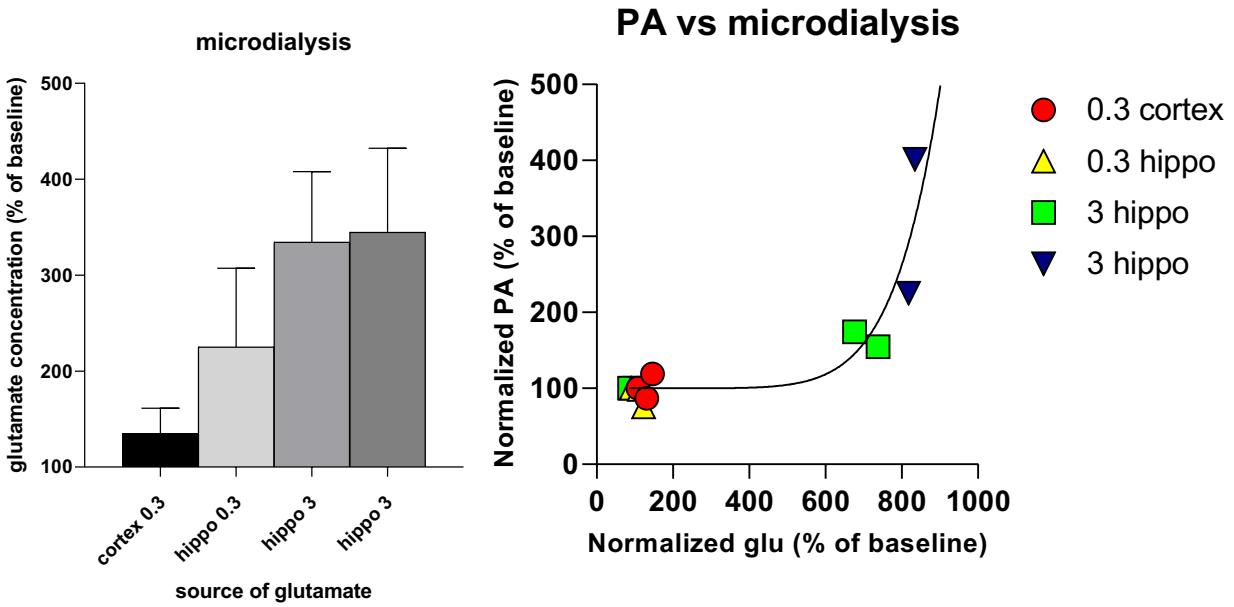

537

538 **Figure 6. Normalized neural activity index (right panel) as a function of extracellular glutamate**
539 **concentration (left panel) at motor cortex and hippocampus.**

540

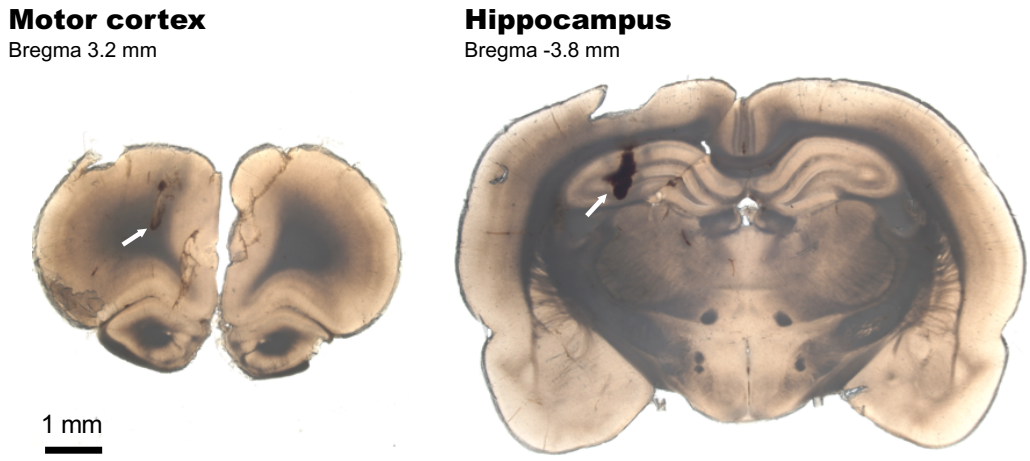

541

542 **Figure 7. Histopathological confirmation of microdialysis probe at motor cortex and hippocampus.** White
543 arrow indicates the wound caused by microdialysis probe installation.

544

545 **Supplementary Material**

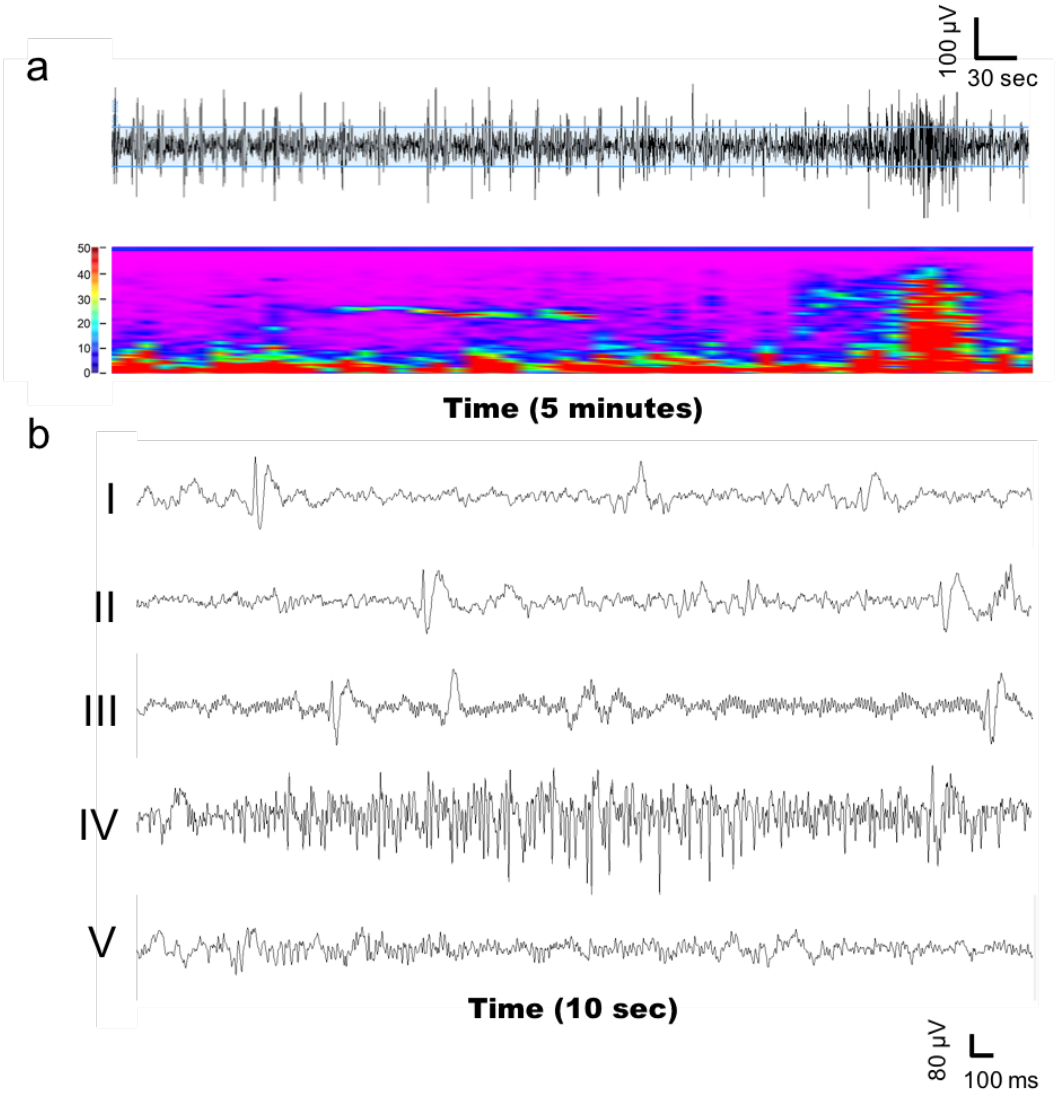

546

547 **Figure S1. Expanded time scale of EEG recording in the hippocampus.** (**a**) Raw trace (5 minutes) shows
548 ramping up of gamma power (see heatmap, 0-50Hz) before onset of focal seizure. (**b**) 10 second expanded time
549 scale of raw EEG traces from hippocampal EEG recording. (I) Baseline (II) immediately after onset of NMDA
550 infusion (III) ramping up of gamma power before seizure event (IV) focal seizure event (V) short duration high
551 frequency hippocampal discharges over the duration of the 20 minute recording (n=1).

552

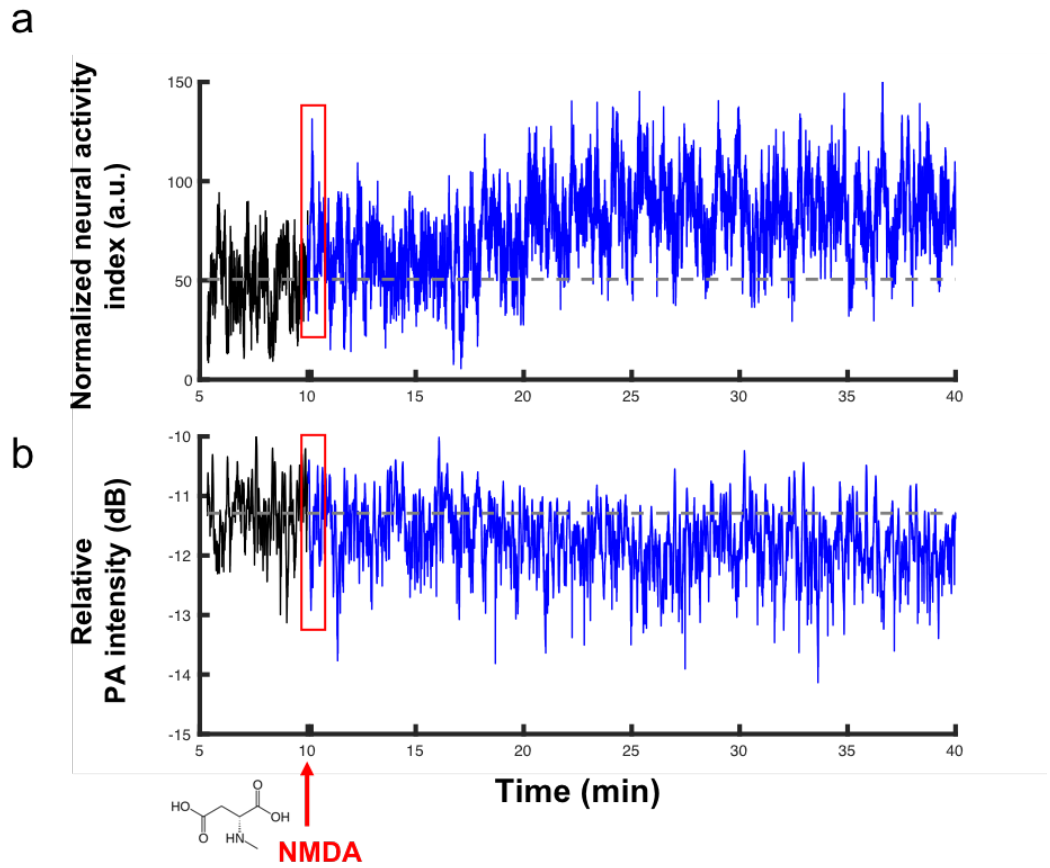

553

554 **Figure S2. PA quantification of a focal seizure with 3 mM NMDA infusion at hippocampus.** (**a**)
555 normalized neural activity index and (**b**) corresponding relative PA intensity traces. Red rectangular indicators
556 show the regions-of-interest used for Figure 5d. Gray dotted lines indicate the basal level measured in baseline
557 phase: 5 – 10 min.

558

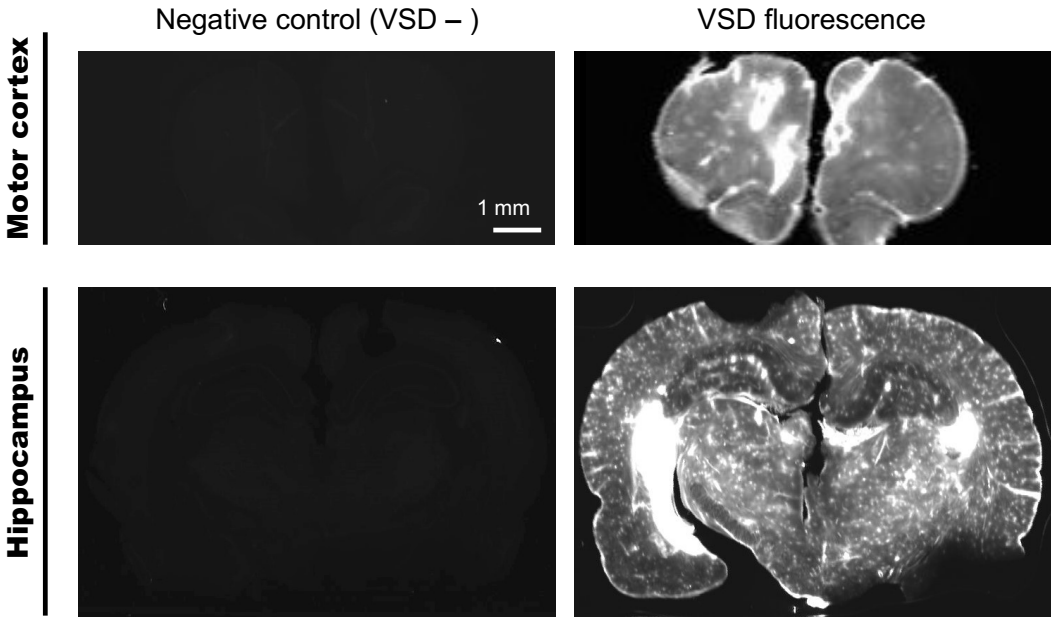

559

560 **Figure S3. Frozen-sectioning histopathological confirmation of systematic VSD delivery through BBB**
561 **using pharmacological modulation.**

562

563 **References**

564 Airan RD, Meyer RA, Ellens NPK, Rhodes KR, Farahani K, Pomper MG, Kadam SD, Green JJ (2017)
565 Noninvasive Targeted Transcranial Neuromodulation via Focused Ultrasound Gated Drug Release
566 from Nanoemulsions. Nano Lett 17:652–659.

567 Andersen P, Holmqvist B, Voorhoeve PE (1966) Entorhinal Activation of Dentate Granule Cells. Acta
568 Physiologica Scandinavica 66:448–460.

569 Ang CW, Carlson GC, Coulter DA (2006) Massive and specific dysregulation of direct cortical input to
570 the hippocampus in temporal lobe epilepsy. J Neurosci 26:11850–11856.

571 Anon (1975) American National Standard for the Safe Use of Lasers. Annals of Internal Medicine
572 82:132.

573 Baumann MH, Ayestas MA, Partilla JS, Sink JR, Shulgin AT, Daley PF, Brandt SD, Rothman RB, Ruoho
574 AE, Cozzi NV (2012) The designer methcathinone analogs, mephedrone and methylone, are
575 substrates for monoamine transporters in brain tissue. Neuropsychopharmacology 37:1192–1203.

576 Chawla MK, Guzowski JF, Ramirez-Amaya V, Lipa P, Hoffman KL, Marriott LK, Worley PF,
577 McNaughton BL, Barnes CA (2005) Sparse, environmentally selective expression of Arc RNA in the
578 upper blade of the rodent fascia dentata by brief spatial experience. Hippocampus 15:579–586.

579 Clay M, Monbouquette HG (2018) A Detailed Model of Electroenzymatic Glutamate Biosensors to Aid
580 in Sensor Optimization and in Applications in Vivo. ACS Chem Neurosci 9:241–251.

581 Connors BW, Malenka RC, Silva LR (1988) Two inhibitory postsynaptic potentials, and GABAA and
582 GABAB receptor-mediated responses in neocortex of rat and cat. The Journal of Physiology
583 406:443–468.

584 Crescenzi R, DeBrosse C, Nanga RPR, Byrne MD, Krishnamoorthy G, D'Aquilla K, Nath H, Morales
585 KH, Iba M, Hariharan H, Lee VMY, Detre JA, Reddy R (2017) Longitudinal imaging reveals
586 subhippocampal dynamics in glutamate levels associated with histopathologic events in a mouse
587 model of tauopathy and healthy mice. Hippocampus 27:285–302.

588 Deán-Ben XL, Sela G, Lauri A, Kneipp M, Ntziachristos V, Westmeyer GG, Shoham S, Razansky D
589 (2016) Functional optoacoustic neuro-tomography for scalable whole-brain monitoring of calcium
590 indicators. Light Sci Appl 5:e16201–e16207.

591 Derdikman D, Hildesheim R, Ahissar E, Arieli A, Grinvald A (2003) Imaging spatiotemporal dynamics
592 of surround inhibition in the barrels somatosensory cortex. J Neurosci 23:3100–3105.

593 Drew KL, Pehek EA, Rasley BT, Ma YL, Green TK (2004) Sampling glutamate and GABA with
594 microdialysis: suggestions on how to get the dialysis membrane closer to the synapse. J Neurosci
595 Methods 140:127–131.

596 Elmore JS, Dillon-Carter O, Partilla JS, Ellefsen KN, Concheiro M, Suzuki M, Rice KC, Huestis MA,
597 Baumann MH (2017) Pharmacokinetic Profiles and Pharmacodynamic Effects for Methylone and Its
598 Metabolites in Rats. Neuropsychopharmacology 42:649–660.

599

600 Gjedde A, Hansen AJ, Quistorff B. Blood-brain glucose transfer in spreading depression. J Neurochem.
601 1981 Oct; 37(4):807-12. PubMed PMID: 7320723

602 Hansen AJ, Quistorff B, Gjedde A. Relationship between local changes in cortical blood flow and
603 extracellular K+ during spreading depression. Acta Physiol Scand. 1980 May; 109(1):1-6. PubMed
604 PMID: 7446156.

605 Homayoun H, Moghaddam B (2007) NMDA receptor hypofunction produces opposite effects on
606 prefrontal cortex interneurons and pyramidal neurons. J Neurosci 27:11496–11500.

607 Hu S (2016) Listening to the Brain with Photoacoustics. IEEE J Select Topics Quantum Electron
608 22:117–126.

609 Hu S, Wang LV (2010) Neurovascular photoacoustic tomography. Front Neuroenergetics 2:10.

610 Hui J, Cao Y, Zhang Y, Kole A, Wang P, Yu G, Eakins G, Sturek M, Chen W, Cheng J-X (2017) Real-
611 time intravascular photoacoustic-ultrasound imaging of lipid-laden plaque in human coronary artery
612 at 16 frames per second. Sci Rep 7:1417.

613 Huynh E, Jin CS, Wilson BC, Zheng G (2014) Aggregate enhanced trimodal porphyrin shell
614 microbubbles for ultrasound, photoacoustic, and fluorescence imaging. Bioconjugate Chem 25:796–
615 801.

616 Ju K-Y, Kang J, Pyo J, Lim J, Chang JH, Lee J-K (2016) pH-Induced aggregated melanin nanoparticles
617 for photoacoustic signal amplification. Nanoscale 8:14448–14456.

618 Kang J, Chung WY, Kang S-W, Kwon HJ, Yoo J, Kim E-K, Chang JH, Song T-K, Lee S, Kwak JY
619 (2014) Ex Vivo Estimation of Photoacoustic Imaging for Detecting Thyroid Microcalcifications
620 Chen X, ed. PLoS ONE 9.

621 Kang J, Kim E-K, Kim GR, Yoon C, Song T-K, Chang JH (2015) Photoacoustic imaging of breast
622 microcalcifications: a validation study with 3-dimensional ex vivo data and spectrophotometric
623 measurement. J Biophoton 8:71–80.

624 Kang J, Zhang HK, Kadam SD, Fedorko J, Valentine H, Kang JU, Rahmim A, Gjedde A, Loew LM,
625 Wong DF, Boctor EM (2017) Transcranial real-time *in vivo* recording of electrophysiological neural
626 activity in the rodent brain with near-infrared photoacoustic voltage-sensitive dye imaging. BioRxiv:
627 1–23.

628 Kang SK, Ammanuel S, Thodupunuri S, Adler DA, Johnston MV, Kadam SD (2018) Sleep dysfunction
629 following neonatal ischemic seizures are differential by neonatal age of insult as determined by
630 qEEG in a mouse model. Neurobiol Dis 116:1–12.

631 Kim GR, Kang J, Kwak JY, Chang JH, Kim SI, Youk JH, Moon HJ, Kim MJ, Kim E-K (2014)
632 Photoacoustic imaging of breast microcalcifications: a preliminary study with 8-gauge core-biopsied
633 breast specimens. Woloschak GE, ed. PLoS ONE 9:e105878.

634 Kondo M, Kobayashi K, Ohkura M, Nakai J, Matsuzaki M (2017) Two-photon calcium imaging of the
635 medial prefrontal cortex and hippocampus without cortical invasion. Elife 6:592.

636 Krnjević K (1997) Role of GABA in cerebral cortex. Can J Physiol Pharmacol 75:439–451.

637 Lauritzen M, Jørgensen MB, Diemer NH, Gjedde A, Hansen AJ. Persistent oligemiaof rat cerebral cortex
638 in the wake of spreading depression. Ann Neurol. 1982 Nov; 12(5):469-74. PubMed PMID:
639 7181451.

640

641 Li W, Chen R, Lv J, Wang H, Liu Y, Peng Y, Qian Z, Fu G, Nie L (2018) In Vivo Photoacoustic
642 Imaging of Brain Injury and Rehabilitation by High-Efficient Near-Infrared Dye Labeled
643 Mesenchymal Stem Cells with Enhanced Brain Barrier Permeability. Adv Sci (Weinh) 5:1700277–11.

644 Liu Y, Yang Y, Sun M, Cui M, Fu Y, Lin Y, Li Z, Nie L (2017) Highly specific noninvasive
645 photoacoustic and positron emission tomography of brain plaque with functionalized croconium dye
646 labeled by a radiotracer. Chem Sci 8:2710–2716.

647 Luke GP, Yeager D, Emelianov SY (2011) Biomedical Applications of Photoacoustic Imaging with
648 Exogenous Contrast Agents. Ann Biomed Eng 40:422–437.

649 McCormick DA (1989) GABA as an inhibitory neurotransmitter in human cerebral cortex. Journal of
650 Neurophysiology 62:1018–1027.

651 Medina-Ceja L, Pardo-Peña K, Morales-Villagrán A, Ortega-Ibarra J, López-Pérez S (2015) Increase in
652 the extracellular glutamate level during seizures and electrical stimulation determined using a high
653 temporal resolution technique. BMC Neurosci 16:11.

654 Moon H, Kang J, Sim C, Kim J, Lee H, Chang JH, Kim H (2015) Multifunctional theranostic contrast
655 agent for photoacoustics- and ultrasound-based tumor diagnosis and ultrasound-stimulated local
656 tumor therapy. Journal of Controlled Release 218:63–71.

657 Moon J-M, Thapliyal N, Hussain KK, Goyal RN, Shim Y-B (2018) Conducting polymer-based
658 electrochemical biosensors for neurotransmitters: A review. Biosens Bioelectron 102:540–552.

659 Nie L, Cai X, Maslov K, Garcia-Uribe A, Anastasio MA, Wang LV (2012) Photoacoustic tomography
660 through a whole adult human skull with a photon recycler. J Biomed Opt 17:110506.

661 Okubo Y, Sekiya H, Namiki S, Sakamoto H, Iinuma S, Yamasaki M, Watanabe M, Hirose K, Iino M
662 (2010) Imaging extrasynaptic glutamate dynamics in the brain. Proceedings of the National Academy
663 of Sciences 107:6526–6531.

664 Paxinos G, Watson C (2014) The Rat Brain in Stereotaxic Coordinates, Seventh edition. Elsevier
665 Academic Press. Available at:
666 https://books.google.com/books?id=FuqGAwAAQBAJ&printsec=frontcover#v=onepage&q&f=
667 false.

668 Petersen CC, Sakmann B (2001) Functionally independent columns of rat somatosensory barrel cortex
669 revealed with voltage-sensitive dye imaging. J Neurosci 21:8435–8446.

670 Petersen CCH, Grinvald A, Sakmann B (2003) Spatiotemporal Dynamics of Sensory Responses in Layer
671 2/3 of Rat Barrel Cortex Measured In Vivo by Voltage-Sensitive Dye Imaging Combined with
672 Whole-Cell Voltage Recordings and Neuron Reconstructions. Journal of Neuroscience 23:1298–
673 1309.

674 Rao B, Zhang R, Li L, Shao J-Y, Wang LV (2017) Photoacoustic imaging of voltage responses beyond
675 the optical diffusion limit. Sci Rep 7:2560.

676 Roberts S, Seeger M, Jiang Y, Mishra A, Sigmund F, Stelzl A, Lauri A, Symvoulidis P, Rolbieski H,
677 Preller M, Deán-Ben XL, Razansky D, Orschmann T, Desbordes SC, Vetschera P, Bach T,
678 Ntziachristos V, Westmeyer GG (2018) Calcium Sensor for Photoacoustic Imaging. J Am Chem Soc
679 140:2718–2721.

680 Sachdev RNS, Krause MR, Mazer JA (2012) Surround suppression and sparse coding in visual and barrel
681 cortices. Front Neural Circuits 6:43.

682 Sherman AD, Hegwood TS, Baruah S, Waziri R (1991) Deficient NMDA-mediated glutamate release
683 from synaptosomes of schizophrenics. Biol Psychiatry 30:1191–1198.

684 Szabo GG, Du X, Oijala M, Varga C, Parent JM, Soltesz I (2017) Extended Interneuronal Network of
685 the Dentate Gyrus. Cell Rep 20:1262–1268.

686 Taube JS, Schwartzkroin PA (1987) Hyperpolarizing responses to application of glutamate in
687 hippocampal CA1 pyramidal neurons. Neuroscience Letters 78:85–90.

688 Voets NL, Hodgetts CJ, Sen A, Adcock JE, Emir U (2017) Hippocampal MRS and subfield volumetry at
689 7T detects dysfunction not specific to seizure focus. Sci Rep: 1–14.

690 Wang LV, Hu S (2012) Photoacoustic tomography: in vivo imaging from organelles to organs. Science
691 335:1458–1462.

692 Wang X, Pang Y, Ku G, Xie X, Stoica G, Wang LV (2003) Noninvasive laser-induced photoacoustic
693 tomography for structural and functional in vivo imaging of the brain. Nat Biotechnol 21:803–806.

694 Weber J, Beard PC, Bohndiek SE (2016) Contrast agents for molecular photoacoustic imaging. Nat Meth
695 13:639–650.

696 Wu M, Springeling G, Lovrak M, Mastik F, Iskander-Rizk S, Wang T, van Beusekom HMM, van der
697 Steen AFW, Van Soest G (2017) Real-time volumetric lipid imaging in vivo by intravascular
698 photoacoustics at 20 frames per second. Biomed Opt Express 8:943–953.

699 Yao J, Maslov KI, Wang LV (2012) In vivo Photoacoustic Tomography of Total Blood Flow and
700 Potential Imaging of Cancer Angiogenesis and Hypermetabolism. Technol Cancer Res Treat 11:301–
701 307.

702 Young AM, Bradford HF (1991) N-methyl-D-aspartate releases excitatory amino acids in rat corpus
703 striatum in vivo. J Neurochem 56:1677–1683.

704 Zhang HF, Maslov K, Stoica G, Wang LV (2006) Functional photoacoustic microscopy for high-
705 resolution and noninvasive in vivo imaging. Nat Biotechnol 24:848–851.

706 Zhang HK, Yan P, Kang J, Abou DS, Le HND, Jha AK, Thorek DLJ, Kang JU, Rahmim A, Wong DF,
707 Boctor EM, Loew LM (2017) Listening to membrane potential: photoacoustic voltage-sensitive dye
708 recording. J Biomed Opt 22:045006.

Zhang P, Li L, Lin L, Hu P, Shi J, He Y, Zhu L, Zhou Y, Wang LV (2018) High-resolution deep functional imaging of the whole mouse brain by photoacoustic computed tomography in vivo. J Biophoton 11:e201700024–e201700026.